The Astrophysical Journal, 994:270 (11pp), 2025 December 1 https://doi.org/10.3847/1538-4357/ae1470

Precision Mass Measurement of ^{26}P and ^{27}S and Their Impact on the ^{26}P(p,γ)^{27}S Reaction in Stellar X-Ray Bursts

Z. Y. Chen[1,2], X. L. Yan[1,8], S. Q. Hou[1,8], J. B. Liu[1,2], J. Y. Shi[1], X. H. Zhou[1], Y. H. Zhang[1], M. Wang[1], X. Zhou[1], M. Zhang[1], H. F. Li[1], M. Z. Sun[1], Y. M. Xing[1], P. Shuai[1], X. Xu[1], W. J. Huang[1,3], Q. Wang[1], Y. N. Song[1], H. Y. Deng[1], H. Y. Jiao[1,2], Y. F. Luo[1,2], Yu. A. Litvinov[4,5], K. Blaum[6], and T. Yamaguchi[7]

[1] State Key Laboratory of Heavy Ion Science and Technology, Institute of Modern Physics, Chinese Academy of Sciences, Lanzhou 730000, People's Republic of China; chenzuyi@impcas.ac.cn, yanxinliang08@impcas.ac.cn, sqhou@impcas.ac.cn
[2] School of Nuclear Science and Technology, University of Chinese Academy of Sciences, Beijing 100049, People's Republic of China
[3] Advanced Energy Science and Technology Guangdong Laboratory, Huizhou 516007, People's Republic of China
[4] GSI Helmholtzzentrum für Schwerionenforschung, Planckstraße 1, 64291 Darmstadt, Germany
[5] Institut für Kernphysik, Universität zu Köln, Zülpicher Str. 77, D-50937 Köln, Germany
[6] Max-Planck-Institut für Kernphysik, Saupfercheckweg 1, 69117 Heidelberg, Germany
[7] Department of Physics, Saitama University, Saitama 338-8570, Japan
Received 2025 July 11; revised 2025 October 13; accepted 2025 October 14; published 2025 December 1

Abstract

Based on the experimental Cooler Storage Ring in Lanzhou, we directly determined the masses of ^{27}S and ^{26}P using $B\rho$-defined isochronous mass spectrometry. The mass excesses were determined to be 17,437(24) keV for ^{27}S and 10,997(10) keV for ^{26}P. These values yield a proton separation energy of 849(26) keV for ^{27}S, representing an eightfold precision improvement over the previous one of 581(214) keV. With precisely measured masses, we evaluated the thermonuclear ^{26}P(p, γ)^{27}S reaction rate under X-ray burst conditions. The updated rate is enhanced within the 0.4–2 GK temperature range, reaching up to 5 times the previous rate at 1 GK. The uncertainty of the reverse ^{27}S(γ, p)^{26}P reaction rate is drastically reduced with the new high-precision mass results, from over 10 orders of magnitude to less than one. We further assessed the impact of the revised rates on the nucleosynthesis in Type I X-ray bursts using a one-zone postprocessing model. The results show that the final abundance ratio of ^{27}S to ^{26}P is increased by about 1 order of magnitude, indicating a more efficient reaction flow toward ^{27}S. Although the sequence ^{25}Si(p, γ)^{26}P(p, γ)^{27}S(β^+)^{27}P is not on the main *rp*-process path, it emerges as a nonnegligible branch contributing to ^{27}P synthesis.

Unified Astronomy Thesaurus concepts: X-ray bursts (1814); Reaction rates (2081); Mass spectrometers (1013); Nuclear physics (2077)

1. Introduction

Astronomical observations reveal that Type I X-ray bursts are among the most frequent thermonuclear explosion phenomena in the Milky Way (A. Parikh et al. 2013; Z. Meisel et al. 2018; D. K. Galloway & L. Keek 2021). These bursts typically occur in binary star systems comprising a neutron star and a companion donor star. The neutron star accretes hydrogen- and helium-rich material from the donor star, forming an accretion layer on its surface. When the temperature and density of the accretion layer reach specific thresholds, thermonuclear reaction runaway is ignited, triggering the X-ray bursts. The ashes of nuclear burning likely remain on the surface and contribute to the chemical composition of the neutron star surface (Z. Meisel et al. 2018). In the environment of X-ray bursts, a series of rapid (p, γ) reactions occurs, in which a nuclide with mass number $A-1$ and atomic number $Z-1$ captures a proton to form the (A, Z) nuclide, accompanied by the release of γ rays. The Q-value of this proton capture reaction equals the proton separation energy S_p of the product nucleus, which is determined by the mass differences of the nuclides involved, $S_p = M(A-1, Z-1) + M(p) - M(A, Z)$. A low or negative proton separation energy characterizes the weakly bound nuclei involved in (p, γ) reactions. Consequently, strong photodisintegration processes establish a dynamic (p, γ) − (γ, p) equilibrium between isotones (H. Schatz et al. 1998). For example, under equilibrium conditions, the abundance ratio between ^{26}P and ^{27}S, resulting from the reaction rate ratio of $N\langle\sigma v\rangle_{p,\gamma}$ to $N\lambda_{\gamma,p}$, is exponentially dependent on the S_p and temperature T:

$$\frac{N(^{27}S)}{N(^{26}P)N(p)} = \frac{\langle\sigma v\rangle_{p,\gamma}}{\lambda_{\gamma,p}} \propto \left(\frac{2\pi k_B T}{h^2}\right)^{3/2} e^{-S_p(^{27}S)/k_B T}, \quad (1)$$

where N is the particle number density, and k_B is the Boltzmann constant. Thus, nuclear masses play a critical role in shaping the rapid proton capture (*rp*) process path.

In the region of neutron-deficient phosphorus and sulfur isotopes, the significance of the ^{26}P(p, γ)^{27}S(β^+)^{27}P branch in the *rp*-process nucleosynthesis pathway has long been a debate. According to H. Schatz (2006), the dominant reaction pathways in this region bypass ^{26}P and ^{27}S through ^{25}Si(β^+)^{25}Al and ^{25}Si(p, α)^{28}P reactions. However, the masses of ^{26}P and ^{27}S were unknown, and the uncertainties of extrapolated proton separation energies (see the following discussion), S_p(^{27}S) and S_p(^{26}P), exceed 200 keV. These large uncertainties introduce significant error bars in relevant

[8] Corresponding author.

reaction rates calculated with statistical models, impeding reliable predictions of nuclear equilibrium near ^{25}Si, and casting doubt on whether the reaction sequence ^{25}Si(p, γ)^{26}P(p, γ)^{27}S(β^+)^{27}P contributes meaningfully to the synthesis of heavier nuclei (A. Parikh et al. 2013).

The Atomic Mass Evaluation (AME2020) predicts mass excess ME(^{26}P) = 10,970(200) keV and ME(^{27}S) = 17,490 (400) keV, respectively. (M. Wang et al. 2021). Based on these estimates, the `ths8` (R. H. Cyburt et al. 2010) nuclear reaction database adopts a proton separation energy of S_p(^{27}S) = 719(357) keV (A. Parikh et al. 2008, 2009). In 2020, L. J. Sun et al. (2020) indirectly determined the ME(^{27}S) = 17,678(77) keV via β-delayed proton emission spectra, yielding an updated S_p(^{27}S) = 581(214) keV. The large uncertainty was dominated by the mass of ^{26}P, which was unknown at that time (M. Wang et al. 2021). In 2023, S. Q. Hou et al. (2023) adopted this S_p(^{27}S) value and calculated the ^{27}S energy levels using experimentally known energy levels in ^{27}Na as a guide. Additionally, they reevaluated the reaction rates of ^{26}P(p, γ)^{27}S and its inverse process, assessing the impact of the reaction rate variations on the *rp*-process in X-ray bursts. The results showed that the updated rate is lower than the previous value reported in `ths8` (R. H. Cyburt et al. 2010), with direct proton capture dominating over resonant contributions. Obviously, the 214 keV error bar in the Q-value (or S_p(^{27}S)) introduces significant uncertainties in the reaction rate and abundance ratio predictions between ^{27}S and ^{26}P, and hinders reliable determination of the *rp*-process pathway (S. Q. Hou et al. 2023).

Recently, we directly measured the masses of ^{26}P and ^{27}S using the Bρ-defined isochronous mass spectrometry ($B\rho$-IMS) with an optimized setting for ^{26}P (Y. Yu et al. 2024). In this work, we report a different experimental setting optimized to achieve maximal transmission efficiency and optimal mass resolution for ^{27}S. The newly obtained mass values are combined with our previous results via weighted averaging, yielding a more precise determination of the two masses. Consequently, the uncertainties in the proton separation energies of ^{26}P and ^{27}S are significantly reduced. Based on the updated nuclear masses obtained, we investigated the impact of these new mass values on the *rp*-process, including the updated forward and reverse reaction rates of ^{26}P(p, γ)^{27}S and evolution of the ^{26}P and ^{27}S abundance over time.

2. $B\rho$-defined Isochronous Mass Spectrometry

The experiment was conducted at the Heavy Ion Research Facility in Lanzhou. The nuclei of interest were generated by bombarding a 10 mm beryllium target with 400 MeV u^{-1} ^{36}Ar^{16+} primary beam at the entrance of the radioactive ion beam line RIBLL2. The forward-emitted fragments were transmitted through RIBLL2 and injected into the Cooler Storage Ring (CSRe) for mass measurements (X. Zhou et al. 2024). The setting of the RIBLL-CSRe system was optimized to ensure both maximal transmission efficiency and optimal mass resolution for ^{27}S^{16+} ions.

Two time-of-flight (TOF) detectors were installed approximately 18 meters apart along the straight section of CSRe (X. L. Yan et al. 2019). As ions circling in the ring, they passed through these detectors once per revolution. When an ion passed through the carbon foil (approximately 100 nm thickness) of a TOF detector, secondary electrons were emitted. These electrons were deflected by an electromagnetic field toward a microchannel plate (MCP), generating fast timing signals (W. Zhang et al. 2014). The TOF signals were fully waveform-sampled by a dual-channel Tektronix oscilloscope (DPO71254C) at a sampling rate of 50 GS s^{-1} for a duration of 400 μs, during which the ions completed approximately 600 revolutions in the ring. Secondary beams were injected into CSRe every 25 s, and a total of approximately 12,000 injections were recorded. Each injection contained about five ions. Offline analysis of the raw waveform data yielded the flying time t_s^i between the two TOF detectors in the straight section and revolution period T_i for each ion (i = 1, 2, 3...) (X. Zhou et al. 2021). The accumulated revolution period spectrum is shown in Figure 1. Details of particle identification using revolution periods can be found in Y. Xing et al. (2019).

2.1. Principle of Mass Measurement

In the storage ring isochronous mass spectrometer, the revolution periods of the stored ions are proportional to the mass-to-charge ratios (m /q) of the ions as

$$\frac{\Delta T}{T} = \frac{1}{\gamma^2}\frac{\Delta m/q}{m/q} + \left(\alpha_p - \frac{1}{\gamma^2}\right)\frac{\Delta B\rho}{B\rho}, \tag{2}$$

where $\gamma = 1/\sqrt{1 - v^2/c^2}$ is the Lorentz factor of ions and α_p is the so-called momentum compaction factor of the storage ring. α_p is a machine parameter defined by the ion-optics of the ring, which establishes the ratio of the relative change in magnetic rigidity ($B\rho$) to the relative change in orbital length (C) (M. Zhang et al. 2022). In the experiment, the magnetic rigidity of CSRe was set such that the Lorentz factor of the ^{27}S^{16+} ions fulfilled the isochronous condition: $\gamma = 1/\sqrt{\alpha_p}$. At this setting, the second term on the right-hand side of Equation (2) vanishes, yielding maximum mass resolving power for ^{27}S^{16+}.

Using reference ions of known mass, $B\rho$-IMS establishes a precalibrated $B\rho(C)$ curve of the storage ring for mass analysis. Upon measuring an ion's revolution period (T) and velocity (v), its mass is interpolated from the curve (M. Zhang et al. 2023; X. Zhou et al. 2024). Velocity v_i of each ion is derived from experimentally measured t_s^i as

$$v_i = \frac{L}{t_s^i + \Delta t_d},\ i = 1, 2, 3..., \tag{3}$$

where L is the straight flight length, and Δt_d is the time delay difference between the signal transmissions from the two TOF detectors to the oscilloscope. The two parameters were offline measured as L = 18,034(1) mm and Δt_d = 99(26) ps, respectively, using laser beams (X. L. Yan et al. 2019). The velocity v_i and magnetic rigidity $B\rho_i$ of the ion are related as

$$B\rho_i = \left(\frac{m}{q}\right)_i \gamma_i v_i . i = 1, 2, 3... \tag{4}$$

Figure 2(a) shows the $B\rho(C_i)$ distribution of the reference ions, with the horizontal axis representing the orbital length C_i = $v_i T_i$. These reference ions were chosen based on two criteria: a mass uncertainty below 20 keV and event counts surpassing 600 in the experiment. Altogether, 11 ion species were utilized to calibrate the $B\rho(C_i)$ curve of the storage ring. To account for the nonlinearity of the curve (M. Zhang et al. 2022, 2023), a seventh-order polynomial was fitted to the $B\rho(C_i)$ data, yielding the best-fit function $B\rho(C_i)_{\rm fit}$. Figure 2(b)

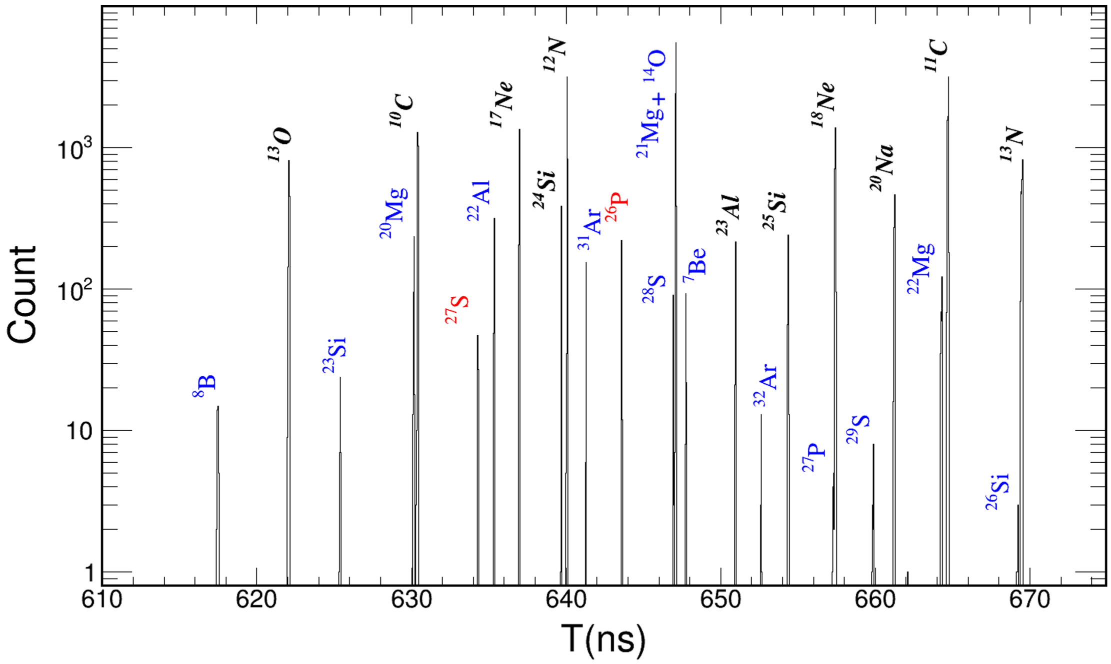

Figure 1. Accumulated revolution period (T) spectrum and the corresponding particle identification. The charge states of all ions are omitted since they are fully stripped. A total of 11 ion species labeled in black act as reference ions for mass calibration. Those labeled in blue are test ions, while those labeled in red denote the target nuclei. More details can be found in the main text.

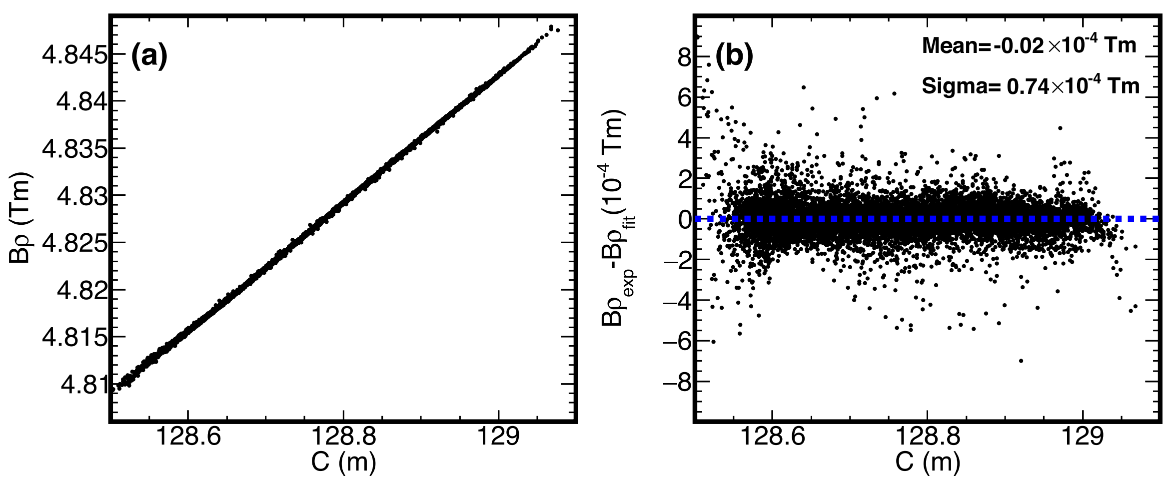

Figure 2. (a) Measured magnetic rigidity $B\rho_i$ (vertical coordinate) and orbit length C_i (horizontal coordinate) using reference ions. (b) Fitting residuals of a seventh-order polynomial.

shows the fitting residuals. Subsequently, for ions of interest, the mass-to-charge ratios are calculated via

$$\left(\frac{m}{q}\right)_i = \frac{B\rho(C_i)_{\rm fit}}{\gamma_i v_i},\ i = 1,\ 2,\ 3... \tag{5}$$

For each ion species, the average m/q value is obtained via a weighted mean and converted to mass excess: $\mathrm{ME} = M - Au$, where A is the mass number and u is the atomic mass unit (M. Wang et al. 2021).

2.2. Velocity Determination of Ions

Assuming that L and Δt_d were constant (M. Zhang et al. 2023) in the event-by-event analysis as discussed above, a systematic correlation between the individual ion mass-to-charge $(m/q)_i$ and its orbit length C_i was observed, as shown by the black data points in Figures 3(a) and (b) for $^{13}O^{8+}$ and $^{13}N^{7+}$, respectively. Such correlated data were fitted by a linear function of $m/q = a + bC$ (see the solid lines in Figures 3(a) and (b)). The fact that slope $b = d(m/q)/dC \neq 0$ for these ions indicates that the calculated velocity v_i from Equation (3) contains a systematic error correlated with C_i. The black points in Figure 3(c) demonstrate that the slope coefficient b for 13 well-resolved ion species has a linear dependence on the average revolution period $\bar{T}$, with a slope $K = d(b)/d\bar{T}$ deviating from zero significantly.

To improve the accuracy of velocity determination, both the flight length L and the signal delay difference Δt_d are treated

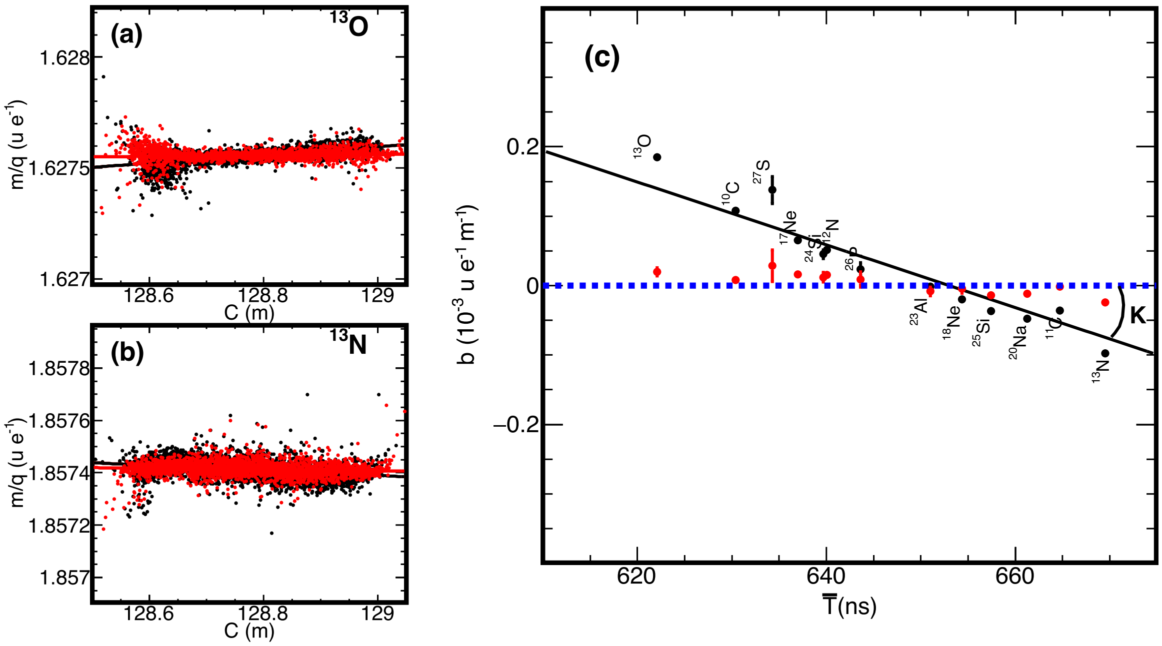

Figure 3. Correlation between $(m/q)_i$ and orbit length C_i for (a) $^{13}O^{8+}$ and (b) $^{13}N^{7+}$. The dependence of slope $b = d(m/q)/dC$ on the average revolution period $\bar{T}$ for different ion species is shown in (c). Black points correspond to constant L and Δt_d; red points correspond to L and Δt_d treated as linear functions of C_i. The solid black lines are the best linear fittings to the corresponding data points.

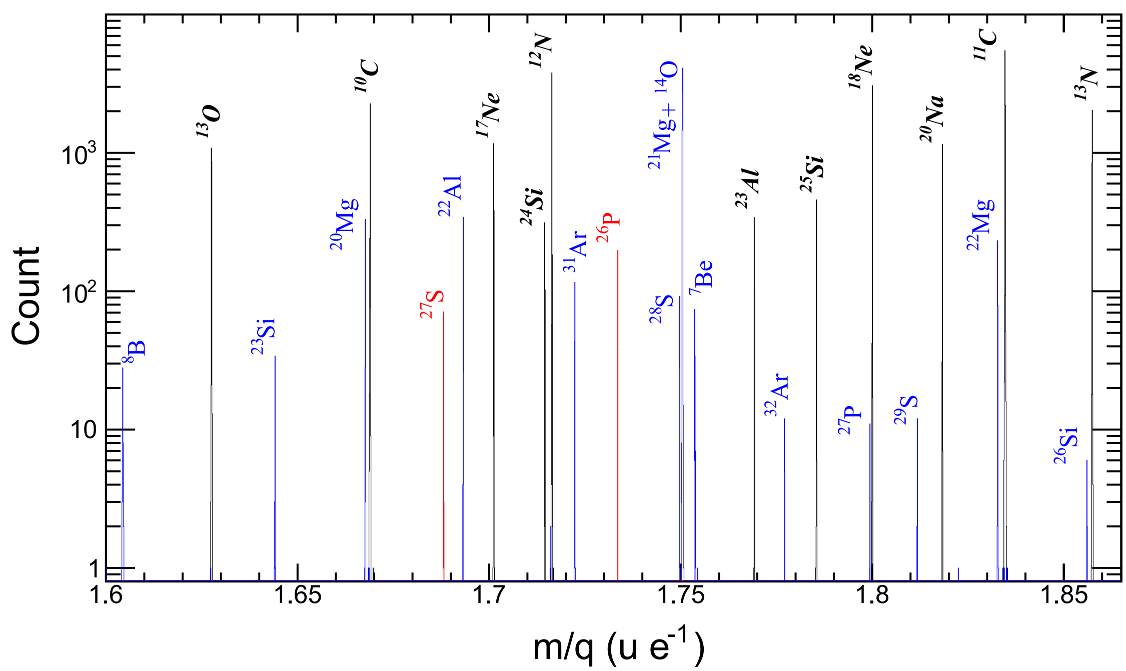

Figure 4. Experimental mass-to-charge m/q spectrum measured in this work. Black peaks represent reference ions used for calibration. Blue peaks are test ions, and red peaks denote the target nuclei.

as functions of C_i (J. Y. Shi et al. 2025, in preparation):

$$L(C_i) = L_0 + L'(C_0)(C_i - C_0),$$
$$\Delta t_d(C_i) = \Delta t_{d0} + \Delta t_d{}'(C_0)(C_i - C_0), \quad i = 1, 2, 3....$$

Here, L_0, Δt_{d0}, $L'(C_0)$, and $\Delta t_d'(C_0)$ are parameters to be calibrated. Nonzero values of $L'(C_0)$ and $\Delta t_d'(C_0)$ reflect variations in flight length and TOF response due to different ion trajectories. These lead to a $d(m/q)/dC$ that correlates with $\bar{T}$. By scanning $L'(C_0)$ and $\Delta t_d'(C_0)$, the optimal parameters minimizing $|K|$ are obtained. Once $L'(C_0)$ and $\Delta t_d'(C_0)$ are fixed, the calculated $(m/q)_i$ becomes independent of C_i, as shown by the red points in Figure 3. Using the method of M. Zhang et al. (2023), the same 11 reference ion species as mentioned above were selected to calibrate L_0 and Δt_{d0}. The optimal parameters minimize the normalized χ_n defined as (M. Wang et al. 2021)

$$\chi_n = \sqrt{\frac{1}{11}\sum_{i=1}^{11} \frac{(\bar{M}_{\rm exp} - M_{\rm AME})_i^2}{(\sigma_{\rm exp}^2 + \sigma_{\rm AME}^2)_i}}. \quad (6)$$

The resulting m/q spectrum is presented in Figure 4.

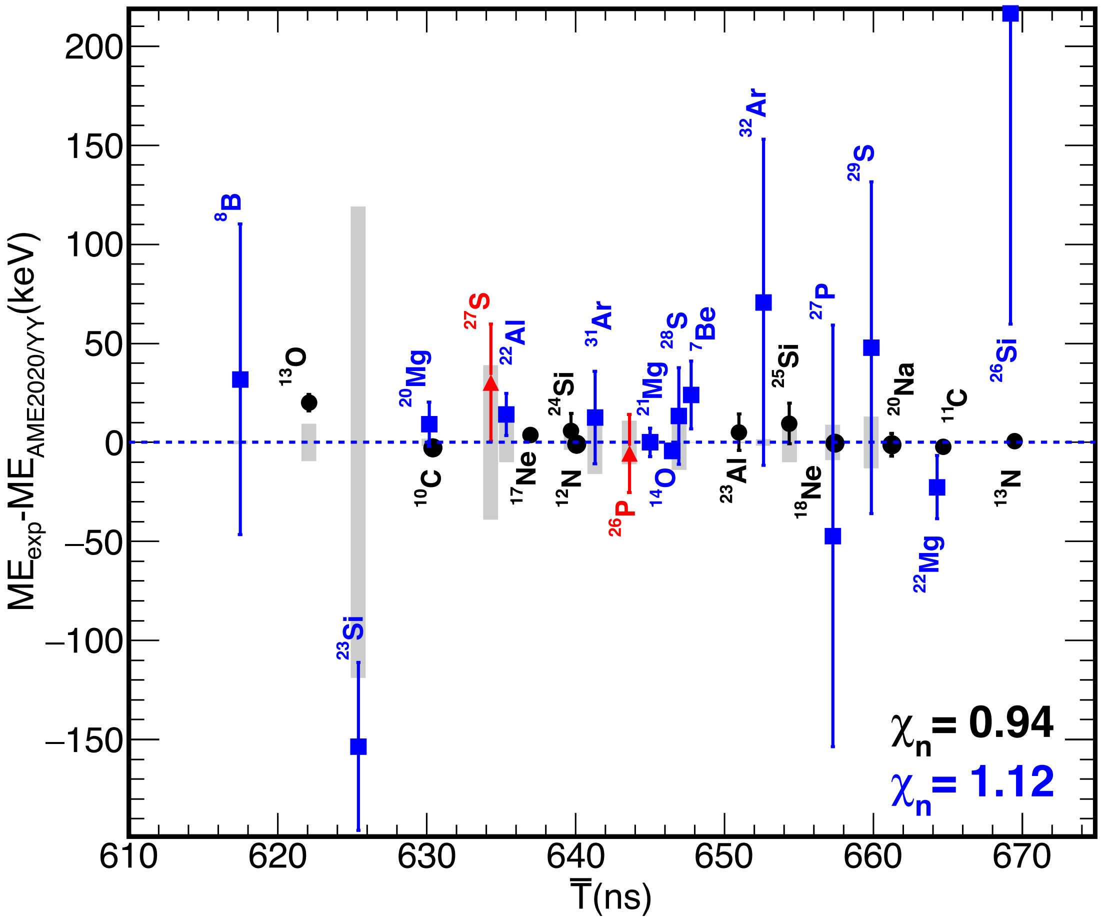

Figure 5. Measured mass excess deviation from the literature values plotted against mean revolution time $\bar{T}$. Black dots represent reference ions used for $B\rho(C)$ calibration and magnetic field correction (M. Zhang et al. 2023); blue dots denote test ions; red dots correspond to the target nuclei of this work. Error bars represent $\pm 1\sigma$ experimental uncertainties, and the gray shaded areas denote the $\pm 1\sigma$ uncertainty ranges from AME2020 (M. Wang et al. 2021) and Y. Yu et al. (2024).

2.3. Discussion of Mass Measurement Results

The comparison of our measured masses with the literature values is shown in Figure 5. In the figure, the black data points represent reference ions used for calibrating $B\rho(C_i)$ and correcting for magnetic field drifts (M. Zhang et al. 2023). The red points correspond to the nuclei of interest, ^{27}S and ^{26}P. The blue points denote test ions whose masses are known, but measured statistics are less than 600. Among test ions, the masses of ^{23}Si, ^{22}Al, ^{31}Ar, and ^{28}S were reported in Y. Yu et al. (2024) and M. Z. Sun et al. (2024), while the rest were taken from the AME2020 database (M. Wang et al. 2021).

For the reference ions, although the mass deviations for ^{13}O, ^{10}C, ^{17}Ne, and ^{11}C slightly exceed 1σ, the overall normalized chi-square value χ_n is 0.94, which is within the expected value of $1 \pm 1/\sqrt{2 \times 11} \approx 1 \pm 0.21$ at 1σ confidence level. As a result, the systematic errors were not considered in the mass calibration.

For the 13 test ions species represented by blue points, the normalized χ_n is 1.12, also within the expected value of $1 \pm 1/\sqrt{2 \times 13} \approx 1 \pm 0.20$. It is worth noting that ME(^{23}Si) = 23,384(42) keV obtained in this work agrees well with more precise results reported recently: ME(^{23}Si) = 23,365(16) keV by Y. M. Xing et al. (2025) and ME(^{23}Si) = 23,363(6) keV by F. M. Maier et al. (2025), providing evidence for the reliability of our measurement results. The measured mass values in this work and Y. Yu et al. (2024) are summarized in Table 1, with weighted average results shown in the sixth column. For the target nuclei ^{27}S and ^{26}P, the measured mass excesses of 17,448(30) keV and 10,992(20) keV are consistent within 1σ uncertainties with the values of 17,418(39) keV and 10,998(11) keV, respectively, reported in Y. Yu et al. (2024). Notably, the mass of ^{27}S was determined with higher precision under the present experimental conditions. The final weighted average mass excess values are 17,437(24) keV for ^{27}S and 10,997(10) keV for ^{26}P.

The mass excess ME(^{27}S) = 17,678(77) keV previously derived indirectly via measurements of the β-delayed two-proton emission (L. J. Sun et al. 2019, 2020) is 241 keV (3.2σ) larger than our direct mass measurement result. Notably, the energy E_{2p} of two-proton emission from the isobaric analog state in ^{27}P to ^{25}Al ground state reported in L. J. Sun et al. (2019, 2020) differs from the other two experimental results by −38(47) keV (V. Borrel et al. 1991) and 93(52) keV (G. Canchel et al. 2001), respectively. These discrepancies in E_{2p} and the inferred ^{27}S mass reflect the limitations of the indirect mass determination method. Based on the new results from this work, the proton separation energy of ^{27}S is determined to be 849(26) keV, larger and more precise than the earlier estimate of 581(214) keV in (L. J. Sun et al. 2020) and the theoretical value of 719(357) keV adopted in `ths8` (R. H. Cyburt et al. 2010). For ^{26}P, a lower limit of $S_p(^{26}\mathrm{P}) > -135$ keV was inferred from γ-ray energy and lifetime measurements of an isomeric state (D. Pérez-Loureiro

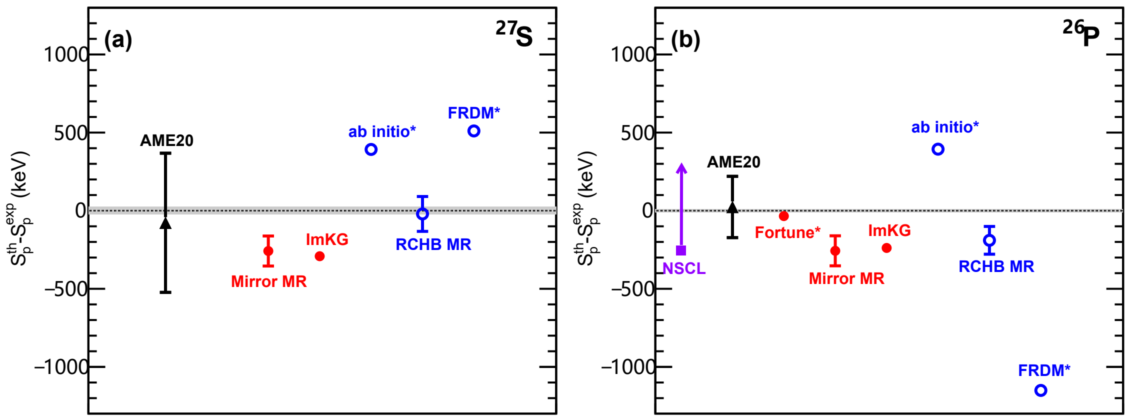

Figure 6. The differences between the results of this work and the theoretical predictions of proton separation energies for ^{26}P and ^{27}S. Red filled circles represent the predictions of local models, blue open circles indicate the predictions of global models, and black filled triangles denote extrapolations in AME2020 (M. Wang et al. 2021). A lower limit of $S_p(^{26}\mathrm{P})$ obtained by an indirect measurement result at NSCL (D. Pérez-Loureiro et al. 2017) is indicated by the purple filled square. Error bars represent respective 1σ uncertainties of mass models. The gray band near zero indicates the $\pm 1\sigma$ uncertainty range of this work. An asterisk (*) indicates models that do not provide uncertainty estimates.

Table 1
Comparison of Measured Ion Counts and Mass Excesses between This Work (Denoted by "exp") and Y. Yu et al. (2024) (Labeled as "YY")

Nucleus (1)	$\mathrm{Count_{exp}}$ (2)	$\mathrm{ME_{exp}}$ (keV) (3)	$\mathrm{Count_{YY}}$ (4)	$\mathrm{ME_{YY}}$ (keV) (5)	$\mathrm{ME_{average}}$ (keV) (6)	$\mathrm{ME_{Lit}}$ (keV) (7)
^{27}S	75	17,448(30)	32	17,418(39)	17,437(24)	17,490#(400#)[a]
^{26}P	236	10,992(20)	284	10,998(11)	10,997(10)	10,970#(200#)[a]
^{23}Si	39	23,384(42)	7	23,537(119)	23,401(49)	23,365(16)[b]
^{22}Al	373	18,117(11)	296	18,103(10)	18,110(7)	18,200#(400#)[a]
^{31}Ar	161	11,303(23)	188	11,290(16)	11,294(13)	11,330#(200#)[a]
^{28}S	121	4191(24)	189	4178(14)	4181(12)	4070(160)[a]

Note. Uncertainties are quoted at the 1σ level. The sixth column presents the weighted average mass excess. The last column presents values from the literature: (a) AME2020; M. Wang et al. (2021); (b) Y. M. Xing et al. (2025). # indicates estimated nonexperimental value.

et al. 2017). Using the directly measured ^{26}P mass in this work and the known mass of ^{25}Si in M. Wang et al. (2021), we determine $S_p(^{26}\mathrm{P}) = 119(15)$ keV, confirming that ^{26}P is proton-bound (Y. Yu et al. 2024).

We further compare the proton separation energies of the target nuclei obtained in this work with predictions from various theoretical mass models, including both local and global models. Local models include mass predictions based on the mirror nuclei separation energy differences (H. T. Fortune 2017, 2018), the empirical mirror mass relations (Y. Y. Zong et al. 2022), and the Improved Kelson–Garvey relation (J. Tian et al. 2013). Global models include the ab initio calculations (S. R. Stroberg et al. 2021), the RCHB model with Coulomb energy analysis (X. W. Xia et al. 2018), and the finite-range droplet macroscopic model (P. Möller et al. 2016). Besides, we also consider the extrapolated values from AME2020 (M. Wang et al. 2021) and the indirect measurement result from NSCL (D. Pérez-Loureiro et al. 2017).

As shown in Figure 6, significant discrepancies are observed between the experimental $S_p(^{27}\mathrm{S})$ and the predictions of the ab initio (S. R. Stroberg et al. 2021) and FRDM models (P. Möller et al. 2016), while AME2020 (M. Wang et al. 2021) and the global RCHB model (X. W. Xia et al. 2018) yield the most accurate predictions. A similar trend is seen for $S_p(^{26}\mathrm{P})$, with the ab initio (S. R. Stroberg et al. 2021) and FRDM (P. Möller et al. 2016) models exhibiting substantial deviations from the measured value, whereas AME2020 (M. Wang et al. 2021) and the local Fortune (H. T. Fortune 2017, 2018) model show good agreement with experimental data. Overall, the comparison suggests that AME2020 and the local model by Fortune et al. (H. T. Fortune 2017, 2018) provide the most reliable mass predictions, whereas the ab initio (S. R. Stroberg et al. 2021) and FRDM (P. Möller et al. 2016) models show pronounced deviations. The directly and precisely determined mass results of short-lived nuclei in this work offer critical benchmarks for validating and improving nuclear mass models.

3. Impact of New Mass Data on Nuclear Reactions in the *rp*-process

Based on the precisely determined proton separation energy of ^{27}S in this work, we reevaluate the forward and reverse reaction rates of the $^{26}\mathrm{P}(p,\gamma)^{27}\mathrm{S}$ reaction, as well as the nuclear reaction pathways of the *rp*-process in the vicinity of ^{25}Si. The evaluation methodology adopted here follows that of S. Q. Hou et al. (2023).

3.1. $^{26}\mathrm{P}(\mathrm{p},\gamma)^{27}\mathrm{S}$ Reaction Rate in X-Ray Burst Environments

The $^{26}\mathrm{P}(p,\gamma)^{27}\mathrm{S}$ reaction rate consists of both resonant and nonresonant contributions (S. Q. Hou et al. 2023). The resonant component originates from the formation of excited resonant states in ^{27}S, and the reaction rate is exponentially dependent on the resonance energy E_r: $N\langle\sigma v\rangle_{\mathrm{res}} \propto \exp(-11.605 E_r/T_9)$

(H. Herndl et al. 1995; C. Iliadis 2007). Changes in the proton separation energy S_p directly affect the resonance energy via $E_r = E_i - S_p$, where E_i is the excitation energy of ^{27}S. According to shell-model calculations in S. Q. Hou et al. (2023), three resonant states are within the Gamow window under typical X-ray burst conditions. These states have excitation energies of 1.685 MeV ($J^{\pi} = 1/2^+$), 2.178 MeV ($9/2^+$), and 2.358 MeV ($7/2^+$). As these excitation energies have not yet been experimentally determined, the shell-model-predicted excitation energies for the mirror nucleus ^{27}Na were used to estimate the uncertainties. The largest deviation between calculated and experimental values in ^{27}Na is 166 keV, which is taken as the uncertainty in the excitation energies of ^{27}S.

Using the newly deduced $S_p(^{27}\mathrm{S})$ from this work, the resonance energies of the three aforementioned states are reduced by 268 keV, yielding updated values of $E_r = 0.836$ MeV ($1/2^+$), 1.329 MeV ($9/2^+$), and 1.509 MeV ($7/2^+$). Furthermore, the uncertainty in the resonance energy is reduced from 271 to 168 keV. The nonresonant component corresponds to the direct capture of a proton by ^{26}P to form the ground state of ^{27}S. This direct proton capture rate is proportional to the effective astrophysical S-factor, S_{eff}, within the Gamow window (C. A. Bertulani 2003; C. Iliadis & M. Wiescher 2004). Previous work (S. Q. Hou et al. 2023) has shown that direct capture dominates the $^{26}\mathrm{P}(p, \gamma)^{27}\mathrm{S}$ reaction rate. In the present study, the updated $S_p(^{27}\mathrm{S})$ is used to recalculate both the resonant and direct capture contributions. The total updated reaction rate for $^{26}\mathrm{P}(p, \gamma)^{27}\mathrm{S}$ is presented in Table 2 and confirms that the direct capture remains dominant (S. Q. Hou et al. 2023).

Figure 7 shows the ratio of the reaction rates calculated in the present work to those given in the commonly used nuclear astrophysics database (Joint Institute for Nuclear Astrophysics Reaction Library database, JINA REACLIB), including `rath` (T. Rauscher & F.-K. Thielemann 2000), `rpsm` (T. Rauscher 1999, private communication), and `ths8` (R. H. Cyburt et al. 2010). Across the entire temperature range, the reaction rate obtained here differs by less than 1 order of magnitude from the estimate in S. Q. Hou et al. (2023). Above 0.04 GK, the present rate is generally lower than that predicted by the statistical models. However, within the 0.4–2 GK temperature range, the new rate exceeds the estimate in S. Q. Hou et al. (2023), reaching a maximum enhancement factor of nearly 5 at 1 GK.

Once the (γ, p) and (p, γ) reactions reach statistical equilibrium, the photodisintegration rate for $^{27}\mathrm{S}(\gamma, p)^{26}\mathrm{P}$ can be calculated via Equation (1) by using the proton capture rate. In comparison with the uncertainty of 214 keV in $S_p(^{27}\mathrm{S})$ adopted in S. Q. Hou et al. (2023), the new mass results reduce this uncertainty to just 26 keV, significantly narrowing the uncertainty in the photodisintegration rate from over 10 orders of magnitude to within 1 order of magnitude, as illustrated in Figure 8. Within the effective temperature range for the *rp*-process (0.1–1 GK), both the reverse reaction rate and its associated uncertainty are substantially reduced. At 0.1 GK, the ^{27}S photodisintegration rate is almost 10^{-14} times the estimate in S. Q. Hou et al. (2023), and at 2 GK it is one-fifth. At 2 GK, the relative uncertainty of this reaction rate is as low as 63%.

3.2. *Investigation of the Nucleosynthesis Pathway in the* rp-*process*

The calculations above have demonstrated the impact of nuclear masses (specifically, proton separation energies) on local reaction rates. To further examine the influence of the newly determined $^{26}\mathrm{P}(p, \gamma)^{27}\mathrm{S}$ reaction rate and its reverse process on the overall nucleosynthesis pathway of the astrophysical *rp*-process, we performed three sets of simulations using the one-zone postprocessing nucleosynthesis network code `ppn` (F. Herwig et al. 2008; P. A. Denissenkov et al. 2014). The adopted temperature-density curve and the initial composition of the accreted matter are consistent with those used in S. Q. Hou et al. (2023) and O. Koike et al. (2004), specifically: $X^0_{\mathrm{H}} = 0.735$, $X^0_{^4\mathrm{He}} = 0.245$, $X^0_{^{14}\mathrm{O}} = 0.007$, and $X^0_{^{15}\mathrm{O}} = 0.013$.

With all other input parameters fixed, the $^{26}\mathrm{P}(p, \gamma)^{27}\mathrm{S}$ and reverse reaction rates were varied in three independent simulations using (a) the statistical model rate from `ths8` (R. H. Cyburt et al. 2010), (b) the rate adopted in S. Q. Hou et al. (2023), and (c) the updated rate determined in this work. Figures 9(a)–(c) present the final mass abundance distribution of isotopes at $t = 100$ s, marking the end of the *rp*-process under each reaction rate scenario. Notably, when employing the updated rate derived from the new mass results, the final abundance of ^{27}S exceeds that predicted by S. Q. Hou et al. (2023) by 1 order of magnitude, and is approximately twice as high as the result using the `ths8` rate (R. H. Cyburt et al. 2010). This substantial enhancement arises primarily from the experimentally determined proton separation energy $S_p(^{27}\mathrm{S}) = 849$ keV, which is significantly larger than both

Table 2
The $^{26}\mathrm{P}(p, \gamma)^{27}\mathrm{S}$ Reaction Rate $N\langle\sigma v\rangle_{p,\gamma}$ (in Units of cm^3 s^{-1} mol^{-1}) as a Function of Temperature T

T (GK) (1)	Low (2)	Median (3)	High (4)
0.01	2.171×10^{-42}	3.448×10^{-42}	5.464×10^{-42}
0.02	5.826×10^{-32}	9.404×10^{-32}	1.494×10^{-31}
0.03	6.698×10^{-27}	1.066×10^{-26}	1.706×10^{-26}
0.04	1.017×10^{-23}	1.643×10^{-23}	2.615×10^{-23}
0.05	1.882×10^{-21}	3.032×10^{-21}	4.845×10^{-21}
0.06	1.006×10^{-19}	1.606×10^{-19}	2.546×10^{-19}
0.07	2.375×10^{-18}	3.792×10^{-18}	6.008×10^{-18}
0.08	3.257×10^{-17}	5.183×10^{-17}	8.123×10^{-17}
0.09	2.912×10^{-16}	4.766×10^{-16}	7.577×10^{-16}
0.10	1.962×10^{-15}	3.177×10^{-15}	5.082×10^{-15}
0.20	1.093×10^{-10}	1.743×10^{-10}	2.817×10^{-10}
0.30	2.216×10^{-8}	3.645×10^{-8}	6.857×10^{-8}
0.40	6.527×10^{-7}	1.133×10^{-6}	4.274×10^{-6}
0.50	7.599×10^{-6}	1.548×10^{-5}	1.253×10^{-4}
0.60	5.252×10^{-5}	1.325×10^{-4}	1.318×10^{-3}
0.70	2.562×10^{-4}	7.661×10^{-4}	6.893×10^{-3}
0.80	9.748×10^{-4}	3.100×10^{-3}	2.326×10^{-2}
0.90	2.981×10^{-3}	9.507×10^{-3}	5.976×10^{-2}
1.00	7.652×10^{-3}	2.368×10^{-2}	1.257×10^{-1}
2.00	7.743×10^{-1}	1.473×10^{0}	3.390×10^{0}
3.00	3.713×10^{0}	6.069×10^{0}	1.102×10^{1}
4.00	7.667×10^{0}	1.203×10^{1}	1.999×10^{1}
5.00	1.126×10^{1}	1.739×10^{1}	2.791×10^{1}
6.00	1.384×10^{1}	2.116×10^{1}	3.381×10^{1}
7.00	1.558×10^{1}	2.374×10^{1}	3.756×10^{1}
8.00	1.677×10^{1}	2.553×10^{1}	3.992×10^{1}
9.00	1.741×10^{1}	2.637×10^{1}	4.121×10^{1}
10.00	1.764×10^{1}	2.675×10^{1}	4.169×10^{1}

Note. Columns (2)–(4), respectively, are the 16th percentile, the 50th percentile (median), and the 84th percentile of the reaction rate at each specified temperature (J. B. Liu et al. 2024).

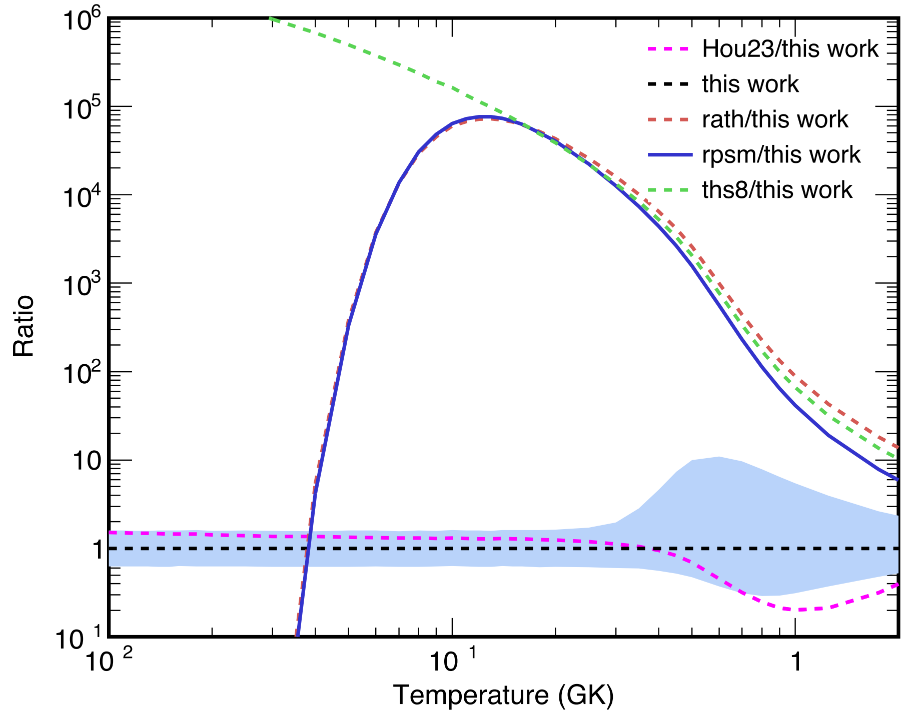

Figure 7. Temperature dependence of the ^{26}P(p, γ)^{27}S reaction rate, $N\langle\sigma v\rangle_{p,\gamma}$. The vertical axis represents the rate ratio between rates in different models and the rate calculated in this work. The blue shaded region denotes the relative uncertainty of the present work; the pink dashed line shows the ratio between the result in S. Q. Hou et al. (2023) and this work; the black dashed line marks the reference ratio of 1.

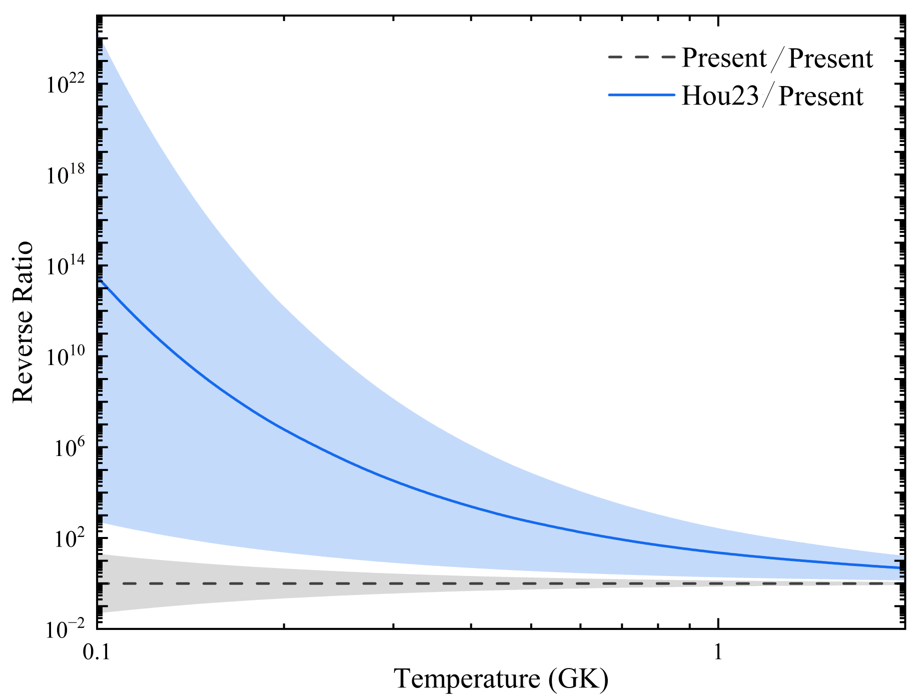

Figure 8. The temperature-dependent behavior of the ratio $R = \lambda_{\gamma,p}(\text{Hou23})/\lambda_{\gamma,p}(\text{this work})$ for the ^{27}S(γ, p)^{26}P photodisintegration rates, contrasting results from S. Q. Hou et al. (2023) with those obtained in this work (blue solid line). The black dashed line marks $R = 1$ for reference. The blue shaded area indicates the uncertainty of $\sigma(\lambda_{\gamma,p})(\text{Hou23})/\lambda_{\gamma,p}(\text{this work})$; the gray shaded region shows the relative uncertainty $\sigma(\lambda_{\gamma,p})(\text{this work})/\lambda_{\gamma,p}(\text{this work})$ obtained in the present work.

the 719 keV used in `ths8` (R. H. Cyburt et al. 2010) and the 581 keV in S. Q. Hou et al. (2023). This suggests that the ^{27}S nucleus is more tightly bound than previously expected, exhibiting increased resistance to proton emission. Consequently, the ^{26}P(p, γ)^{27}S reaction suppresses the reverse photodisintegration reaction ^{27}S(γ, p)^{26}P, allowing the reaction flow to proceed less impeded from ^{26}P to ^{27}S, thereby enhancing the final ^{27}S yield.

Figure 10 further illustrates the time evolution of the abundance ratio ^{27}S/^{26}P during the rp-process. Compared with the rate adopted in S. Q. Hou et al. (2023), the reaction rate based on the newly determined masses (i.e., the higher $S_p(^{27}\text{S})$)

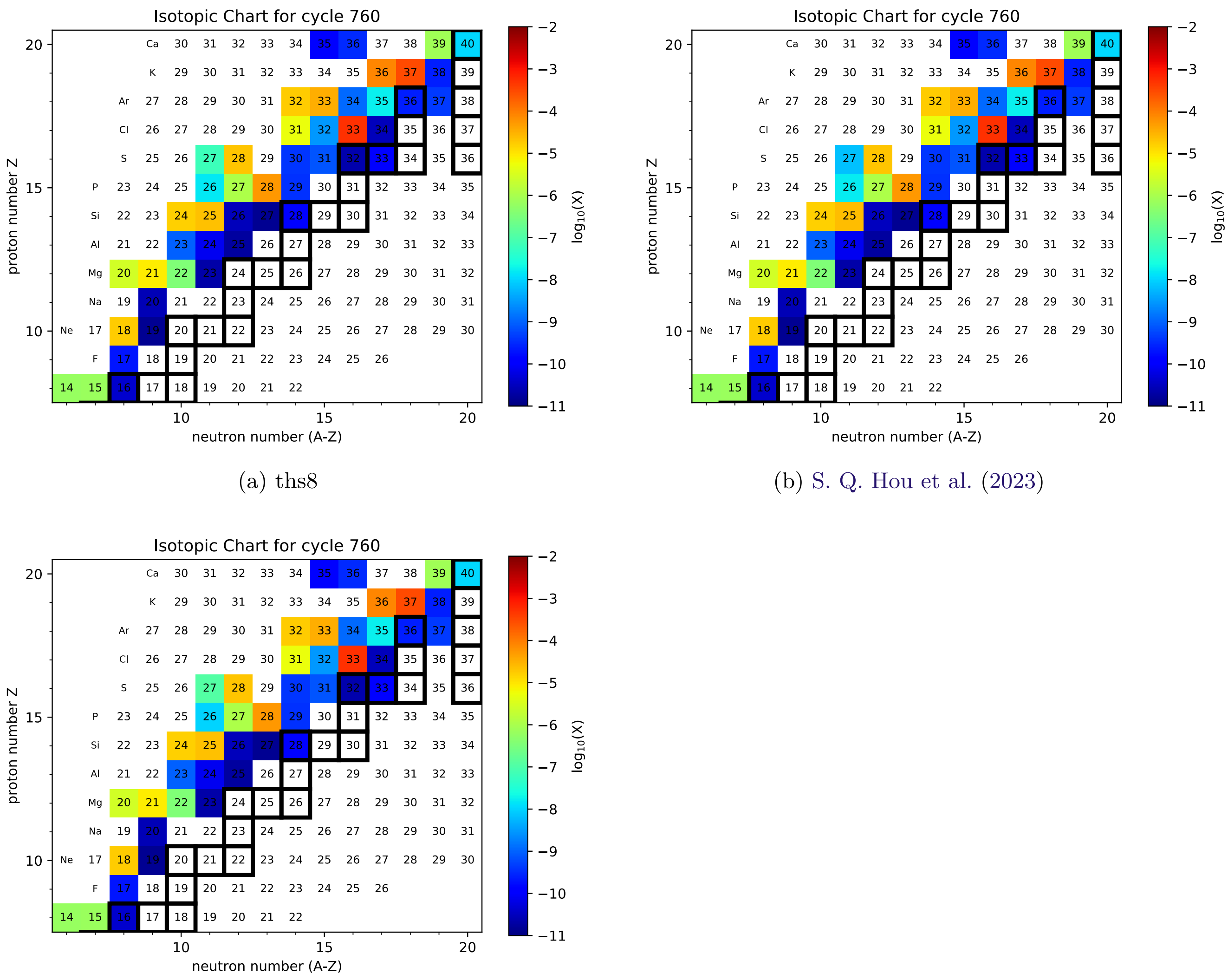

(a) ths8

(b) S. Q. Hou et al. (2023)

(c) this work

Figure 9. Mass abundance distribution log(X) of reaction products at the end of the *rp*-process (t = 100 s) on the nuclear chart. (a) Using the ths8 reaction rate (R. H. Cyburt et al. 2010); (b) using the rate from S. Q. Hou et al. (2023); (c) using the updated rate from this work. Black empty squares represent stable isotopes.

leads to an increase by a factor of about 10 in the accumulation of matter at ^{27}S. This means more material flows through ^{26}P(p, γ)^{27}S in the *rp*-process. Eventually, the synthesized ^{26}P and ^{27}S during the *rp*-process decay back to stable isotopes ^{26}Mg and ^{27}Al, respectively. After full decay, the elemental abundances of the *rp*-process products (burning ashes) are shown in Figure 11. There is only one stable isotope of aluminum (^{27}Al), while there are three stable isotopes of magnesium (^{24,25,26}Mg). Relative to the results from S. Q. Hou et al. (2023), our work shows that the abundance of aluminum (^{27}Al) was increased by about 8.9% while the abundance of magnesium was reduced by about 2.0%. The abundances of other elements were not affected. These results show that the reaction sequence ^{25}Si(p, γ)^{26}P(p, γ)^{27}S(β^+)^{27}P represents a nonnegligible branching path contributing to the synthesis of ^{27}P in the *rp*-process.

4. Summary and Outlook

Using the isochronous mass spectrometry technique at the Heavy Ion Storage Ring in Lanzhou, we have measured the masses of several nuclei with improved precision, including ^{27}S and ^{26}P. We determined the proton separation energy of ^{27}S to be $S_p = 849 \pm 26$ keV, which is 130 to 368 keV larger than the previous estimates, with an uncertainty only one-eighth of that reported earlier. The experimental mass values and resulting proton separation energies were compared with various theoretical models and indirect measurement results. Among them, the AME2020 evaluation (M. Wang et al. 2021) and the local mass model proposed by H. T. Fortune (2017, 2018), based on mirror separation energy differences, show the best agreements with our results for both ^{26}P and ^{27}S. In contrast, the ab initio mass predictions (S. R. Stroberg et al. 2021) exhibit significant discrepancies from our experimental results.

Leveraging the updated mass data, we recalculated the thermonuclear reaction rates for the ^{26}P(p, γ)^{27}S and its inverse reaction under X-ray burst conditions. Across the temperature range of 0.01–2 GK, the updated (p, γ) rate is about 0.5 (or 5) times the rate reported in S. Q. Hou et al. (2023) below (or above) 0.4 GK. The reverse rate, ^{27}S(γ, p), was significantly suppressed, with its relative uncertainty reduced from 10 orders of magnitude to within a factor of 10. Nucleosynthesis network calculations indicate that the larger S_p(^{27}S) substantially enhances the proton capture probability of ^{26}P, leading to

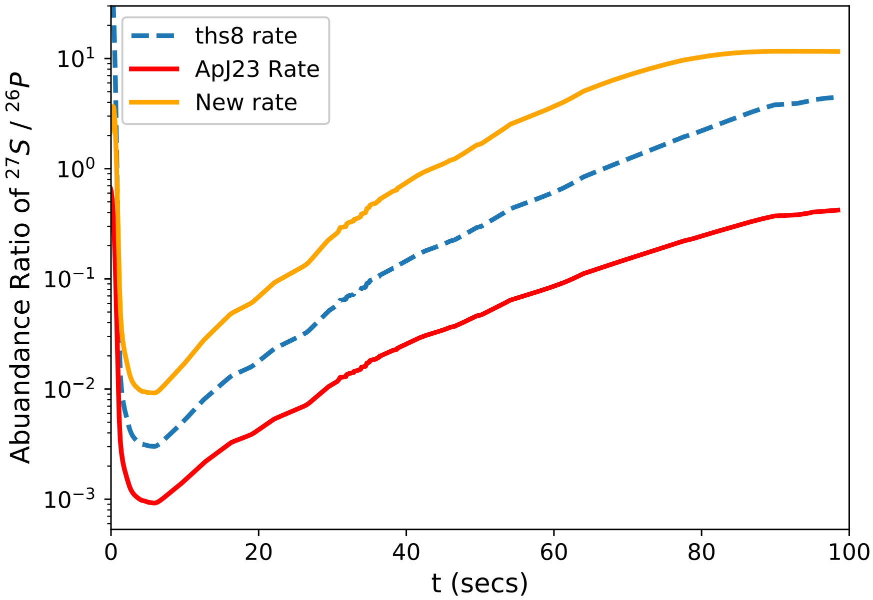

Figure 10. Time evolution of the $^{27}S/^{26}P$ abundance ratio during the *rp*-process. The blue dashed line corresponds to results using the reaction rate from S. Q. Hou et al. (2023), the red solid line shows the outcome using the `ths8` rate (R. H. Cyburt et al. 2010), and the orange solid line represents the results obtained using the updated rate from this study.

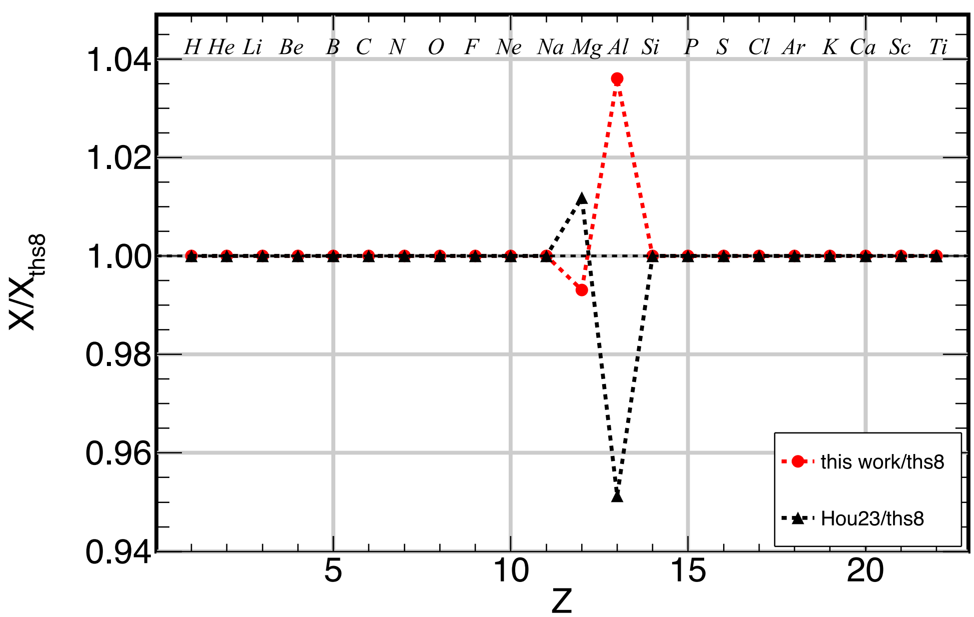

Figure 11. Comparison of final elemental abundances after full decay. The abundance ratio on the *y*-axis is normalized to the results using reaction rate from ths8 (R. H. Cyburt et al. 2010). Red solid circles denote results of this work, while black triangles correspond to the results from S. Q. Hou et al. (2023). ^{26}P and ^{27}S decay back to stable isotopes ^{26}Mg and ^{27}Al, respectively.

an increase of about 1 order of magnitude in the $^{27}S/^{26}P$ abundance ratio produced in the *rp*-process. Although the reaction sequence $^{25}Si(p, \gamma)^{26}P(p, \gamma)^{27}S(\beta^+)^{27}P$ is not on the main *rp*-process pathway, its contribution to the production of ^{27}P is nonnegligible. Our high-precision mass results and the corresponding reaction rate updates provide more reliable input for astrophysical reaction networks, thereby advancing our understanding of the *rp*-process and the mechanisms of X-ray bursts. Currently, within the reaction chain $^{25}Si(p, \gamma)^{26}P(p, \gamma)^{27}S(\beta^+)^{27}P$, the resonant structure of ^{27}S remains as the major uncertainty, lacking experimental data. We therefore recommend future high-precision spectroscopy of ^{27}S to further constrain theoretical models of X-ray bursts.

Acknowledgments

This work was supported by the National Key R&D Program of China (grants Nos. 2023YFA1606401, 2021YFA1601500, and 2022YFA1603300), the Youth Innovation Promotion Association of the Chinese Academy of Sciences (grants Nos. 2021419 and 2022423), the Research Program of State Key Laboratory of Heavy Ion Science and Technology, Institute of Modern Physics, Chinese Academy of Sciences, under grant No. HIST2025CS05, the Youth Program for Regional Development of the Chinese Academy of Sciences (grant No. [2023]15), the Youth Team Program of the Chinese Academy of Sciences for Stable Support of Basic Research Fields (grant No. YSBR-002), the National Natural Science Foundation of China (grant Nos.

12135017, 12121005, 12322507, 12305126, and 12305151), Science and Technology Leading Talent Foundation of Gansu Province (grant No. 25RCKA025), the Talent Support Project of Guangdong Program (No. 2023TQ07A872), the Longyuan Youth Talent Program of Gansu Province, the Major Science and Technology Projects in Gansu Province (No. 24GD13GA005), Gansu Youth S&T Tackling Key Problems Project (Project-Unveiling and Leader-Appointing Mechanism) (GQK2024058), and the Gansu Natural Science Foundation (grant No. 24JRRA036). Y.H.Z. acknowledges support from the ExtreMe Matter Institute EMMI at the GSI Helmholtzzentrum für Schwerionenforschung, Darmstadt, Germany.

Author Contributions

M.Z. and M.W. codesigned the experiments. X.L.Y. managed the experimental campaign, while M.W. directed project organization. Data analysis was performed by Z.Y.C., X.Z., J.Y.S., X.L.Y., and Y.H.Z. Astrophysical interpretations were led by J.B.L. and S.Q.H. The manuscript's first draft was written by Z.Y.C., S.Q.H., and X.L.Y. All authors participated in the experiments and manuscript revision.

ORCID iDs

X. L. Yan https://orcid.org/0000-0001-6399-096X
S. Q. Hou https://orcid.org/0000-0001-9182-0853
M. Wang https://orcid.org/0000-0003-2408-8089
Y. M. Xing https://orcid.org/0000-0002-9879-8983
X. Xu https://orcid.org/0000-0002-8148-3539
Yu. A. Litvinov https://orcid.org/0000-0002-7043-4993
K. Blaum https://orcid.org/0000-0003-4468-9316

References

Bertulani, C. A. 2003, CoPhC, 156, 123
Borrel, V., Jacmart, J., Pougheon, F., et al. 1991, NuPhA, 531, 353
Canchel, G., Achouri, L., Äystö, J., et al. 2001, EPJA, 12, 377
Cyburt, R. H., Amthor, A. M., Ferguson, R., et al. 2010, ApJS, 189, 240
Denissenkov, P. A., Truran, J. W., Pignatari, M., et al. 2014, MNRAS, 442, 2058
Fortune, H. T. 2017, PhRvC, 96, 034304
Fortune, H. T. 2018, PhRvC, 97, 034301
Galloway, D. K., & Keek, L. 2021, ASSL, 461, 209
Herndl, H., Görres, J., Wiescher, M., Brown, B. A., & Van Wormer, L. 1995, PhRvC, 52, 1078
Herwig, F., Diehl, S., Fryer, C. L., et al. 2008, in Proc. 10th Symp. Nuclei in the Cosmos (NIC X) (SISSA), 23
Hou, S. Q., Liu, J. B., Trueman, T. C. L., et al. 2023, ApJ, 950, 133
Iliadis, C. 2007, Nuclear Physics of Stars (Wiley)
Iliadis, C., & Wiescher, M. 2004, PhRvC, 69, 064305
Koike, O., Hashimoto, M., Kuromizu, R., & Fujimoto, S. 2004, ApJ, 603, 242
Liu, J. B., José, J., Hou, S. Q., et al. 2024, A&A, 687, A199
Maier, F. M., Bollen, G., Brown, B. A., et al. 2025, PhRvC, 112, 014329
Meisel, Z., Deibel, A., Keek, L., Shternin, P., & Elfritz, J. 2018, JPhG, 45, 093001
Möller, P., Sierk, A., Ichikawa, T., & Sagawa, H. 2016, ADNDT, 109, 1
Parikh, A., José, J., Iliadis, C., Moreno, F., & Rauscher, T. 2009, PhRvC, 79, 045802
Parikh, A., José, J., Moreno, F., & Iliadis, C. 2008, ApJS, 178, 110
Parikh, A., José, J., Sala, G., & Iliadis, C. 2013, PrPNP, 69, 225
Pérez-Loureiro, D., Wrede, C., Bennett, M. B., et al. 2017, PhRvC, 96, 014306
Rauscher, T., & Thielemann, F.-K. 2000, ADNDT, 75, 1
Schatz, H. 2006, IJMSp, 251, 293
Schatz, H., Aprahamian, A., Görres, J., et al. 1998, PhR, 294, 167
Stroberg, S. R., Holt, J. D., Schwenk, A., & Simonis, J. 2021, PhRvL, 126, 022501
Sun, L. J., Xu, X. X., Hou, S. Q., et al. 2020, PhLB, 802, 135213
Sun, L. J., Xu, X. X., Lin, C. J., et al. 2019, PhRvC, 99, 064312
Sun, M. Z., Yu, Y., Wang, X. P., et al. 2024, ChPhC, 48, 034002
Tian, J., Wang, N., Li, C., & Li, J. 2013, PhRvC, 87, 014313
Wang, M., Huang, W., Kondev, F., Audi, G., & Naimi, S. 2021, ChPhC, 45, 030003
Xia, X. W., Lim, Y., Zhao, P. W., et al. 2018, ADNDT, 121, 1
Xing, Y., Zhang, Y., Wang, M., et al. 2019, NIMPA, 941, 162331
Xing, Y. M., Luo, Y. F., Zhang, Y. H., et al. 2025, PhRvL, 135, 012501
Yan, X. L., Chen, R.-J., Wang, M., et al. 2019, NIMPA, 931, 52
Yu, Y., Xing, Y. M., Zhang, Y. H., et al. 2024, PhRvL, 133, 222501
Zhang, M., Zhang, Y., Wang, M., et al. 2022, NIMPA, 1027, 166329
Zhang, M., Zhou, X., Wang, M., et al. 2023, EPJA, 59, 27
Zhang, W., Tu, X., Wang, M., et al. 2014, NIMPA, 756, 1
Zhou, X., Wang, M., Yuan, Y.-J., et al. 2021, NuScT, 32, 37
Zhou, X., Wang, M., Zhang, Y.-H., et al. 2024, NuScT, 35, 213
Zong, Y. Y., Ma, C., Lin, M. Q., & Zhao, Y. M. 2022, PhRvC, 105, 034321